Geoelectrical and hydro-chemical monitoring of karst formation at the laboratory scale

Flore Rembert[1], Marie Leger[2], Damien Jougnot[3], and Linda Luquot[2]

[1]Univ. Orléans, CNRS, BRGM, ISTO, UMR 7327, Orléans, F-45071, France
[2]Géosciences Montpellier, Univ Montpellier, CNRS, Univ Antilles, Montpellier, France
[3]Sorbonne Université, CNRS, EPHE, METIS, F-75005, Paris, France

Correspondence: Flore Rembert (flore.rembert@univ-orleans.fr)

Abstract. Ensuring sustainable strategies to manage water resources in karst reservoirs requires a better understanding of the mechanisms responsible for ~~conduits formation~~ dissolution features in the rock mass and the development of detection methods for these hydrological and geochemical processes. In this study, we monitored the electrical conductivity of two limestone core samples during controlled dissolution experiments. We interpret the results with a physics-based model describing the porous medium as effective structural parameters that are tortuosity and constrictivity. We obtain that ~~constrictivity is more affected by calcite dissolution compared to tortuosity~~ the electrical signature of calcite dissolution is more impacted by the evolution of constrictivity than by tortuosity, as commonly supposed. Based on our experimental results and data sets from the literature, we show that the characteristic Johnson length is a valuable structural witness of calcite dissolution impact linking electrical and hydrological properties.

Short summary. The formation of underground cavities, called karsts, resulting from carbonate rock dissolution, is at stake in many environmental and societal issues, notably through risk management and the administration and quality of drinking water resources. Facing natural environment complexity, we propose a laboratory study combining hydro-chemical monitoring, 3D imaging, and non-invasive observation of electrical properties, showing the benefits of geoelectrical monitoring to map karst formation.
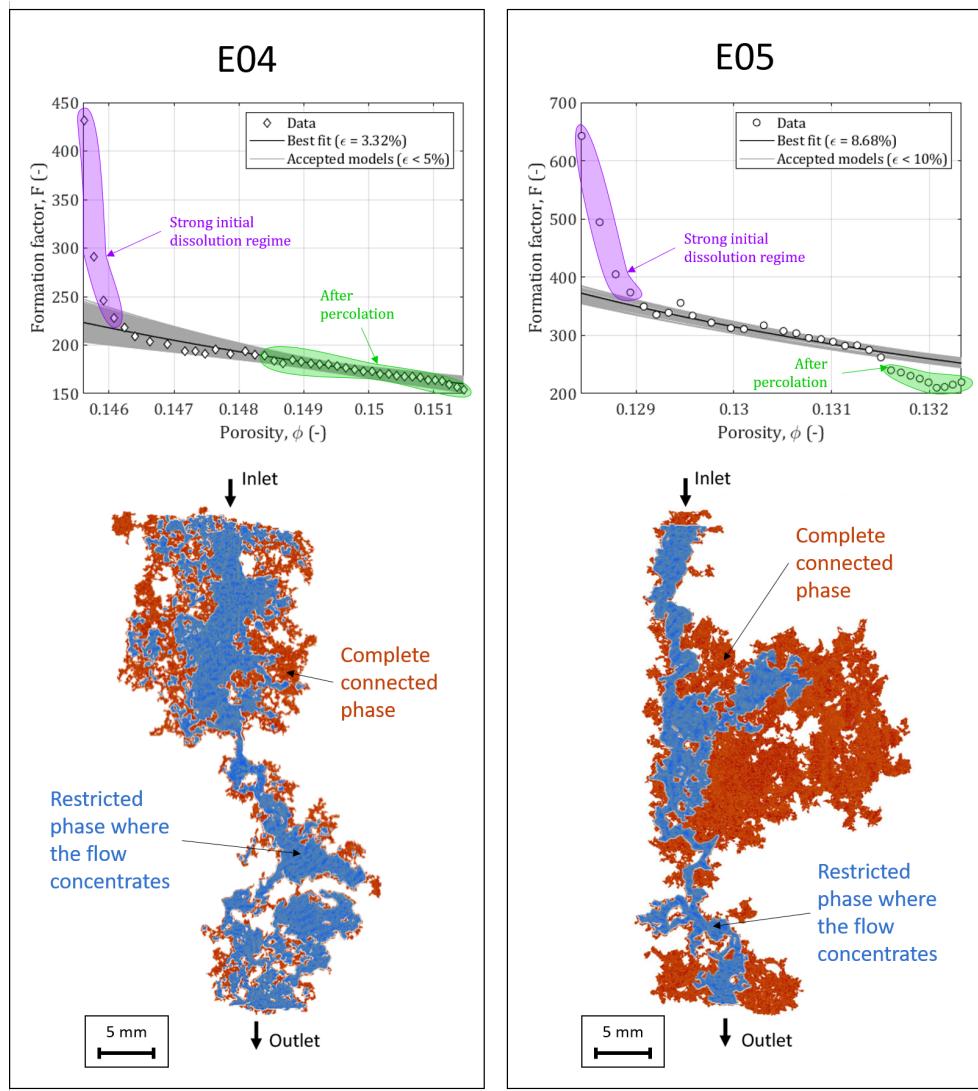
Figure 0. Graphical abstract

1 Introduction

Carbonate rocks occupy a vast area on the Earth's surface (Chen et al., 2017) and constitute reservoirs for key resources such as groundwater (e.g., Kačaroğlu, 1999; Bakalowicz, 2005), geothermal energy (e.g., Montanari et al., 2017), or fossil energies (e.g., Burchette, 2012). The study of carbonate rocks is also very active because of their potential to serve for carbon dioxide (CO$_2$) geologic sequestration (e.g., Luquot and Gouze, 2009; Cherubini et al., 2019). Carbonate rocks are also well known to be linked to coastal or agricultural issues ~~with~~ related to contamination, erosion, and landsliding, to civil engineering with

risks of cavity presence and collapsing, but also as a commonly exploited noble building material (e.g., Drew et al., 2017; Buckerfield et al., 2020). Investigating carbonate reservoirs is a crucial challenge due to the multi-scale heterogeneity of rock properties and their strong chemical reactivity (e.g., Choquette and Pray, 1970; Lønøy, 2006). These features are responsible

25 for specific processes occurring in carbonate rocks over a wide size range (nm to km), such as groundwater flow and ionic transport in a reactive porous medium (e.g., Ford and Williams, 2013).

Dissolution of carbonate samples caused by CO_2 or acid solution injection has already been well studied in the laboratory to understand the formations of conduits and their intricate coupling with transport properties such as permeability and porosity (e.g., Golfier et al., 2002; Noiriel et al., 2004, 2005; Rötting et al., 2015). However,

30 these experiments generally rely on image analysis, an accurate laboratory work technique that cannot be used in the field. Additionally, in a subsurface context, chemical analysis of the pore water can be quite intrusive, providing only restricted and spatially limited information (e.g., Goldscheider et al., 2008). Thus, studying large-scale heterogeneities such as karst environments can benefit from the use of non-invasive tools such as the ones proposed in hydrogeophysics (e.g., Hubbard and Linde, 2011; Binley et al.,

35 2015). In particular, geoelectrical methods are good candidates to detect the emergence of karstification related to the heterogeneous dissolution of large volumes (e.g., Liñán Baena et al., 2009; Chalikakis et al., 2011; Meyerhoff et al., 2014; Kaufmann and Romanov, 2016) since they present a high sensitivity to physical and chemical properties of both porous matrix and interstitial fluids (e.g., Glover, 2015). An increasing amount of work has shown the interest and the effectiveness of geoelectrical methods for laboratory or in situ monitoring of pore space

40 description, hydrological processes, and contaminant transport (e.g., Revil et al., 2012; Garing et al., 2014; Jougnot et al., 2018; Ben Moshe et al., 2021; Sun et al., 2021; Koohbor et al., 2022). Studies on the geoelectrical monitoring of calcite precipitation and dissolution processes are emerging, highlighting the interest of these methods for non-intrusive characterizations (e.g., Wu et al., 2010; Zhang et al., 2012; Leroy et al., 2017; Cherubini et al., 2019; Niu and Zhang, 2019; Saneiyan et al., 2019, 2021; Izumoto et al., 2020, 2022; Rembert et al., 2022). Nevertheless, geophysical methods are indirect,

45 and thus, require appropriate models to give a quantitative interpretation (e.g., Binley and Kemna, 2005; Kemna et al., 2012).

The present work attempts to give some answers on how the electrical signal is impacted by conduit formation in limestone due to calcite dissolution, and how the electrical properties can be related to evolving structural parameters. To this end, acid injections are conducted on two core samples of the same limestone at atmospheric conditions and under two different flow rates. The samples used in this study come from a broad data set, for which two studies have already been published. First, the study of

50 Leger and Luquot (2021) focuses on multimodal petrophysical and structural characterization of the samples. Then, Leger et al. (2022a) analyzes, and compares with the initial and final characterization of the samples with laboratory methods and coupled CT scan imaging, the evolution of porosity and permeability of the samples during dissolution experiments creating the formation

55 of preferential conduits. This small-scale approach to heterogeneous dissolution is an analog of the natural processes involved

in forming conduits by dissolution leading to karstification. The results of this study are transferable to large-scale applications (e.g., karst formation, CO_2 geological storage, and geothermal energy).

In the present study, in addition to chemical and hydrodynamic properties, the electrical conductivity of the sample is also recorded during the dissolution. The analysis of the evolution of the monitored properties and their comparison with the initial ~~conditions, is analyzed in order to observe in~~ and final characterizations of the samples enables observing in which proportion they are ~~responsible for the changes induced~~ affected by the acid ~~flowing through the rock~~percolation. Then, we focus on the electrical conductivity interpretation and apply a physics-based model that conceptualizes the porous medium as sub-parallel tortuous capillaries, which follow a pseudo-fractal size distribution and present sinusoidal variations of their aperture. Finally, we compare the electrical conductivity results of this study with experimental and numerical data sets from the literature.

2 Materials and Methods

2.1 Samples properties and petrophysical characterization

The two core samples of this study are part of a wider published data set ~~(Leger and Luquot, 2021; ?)~~(Leger and Luquot, 2021; Leger et al., . They were cored into an Oxfordian crinoid limestone from the Euville quarry in Nancy, France. The two samples are named E04 and E05. The cores have a length of 32 and $31\,\mathrm{mm}$, respectively, and a diameter of $18\,\mathrm{mm}$. They are surrounded with epoxy resin and PVC pipe for a total diameter of $25\,\mathrm{mm}$ (i.e., one inch).

Measurements of X-ray Diffraction (XRD) on a Bruker D8 Discover ~~,~~and X-ray Fluorescence (XRF) ~~measurements~~ on an FEI Quanta 200 FEG show that these rock samples are fully composed of calcium carbonate ($CaCO_3$). To characterize the cores samples' structure, petrophysical measurements are done by non-destructive laboratory methods: porosity ϕ (–), permeability k (m^2), and electrical conductivity σ ($\mathrm{S\,m}^{-1}$) on saturated samples at different salinities~~to~~. These petrophysical characterizations were carried out on dry and saturated samples using four different fluids in chemical equilibrium with the samples at four sodium chloride (NaCl) concentrations: 0.3, 0.2, 0.1, and $0.05\,\mathrm{mol\,L}^{-1}$. The samples were dried in an oven between each saturation with the different NaCl concentrations. Gas porosity and permeability were measured by helium injection using a porosimeter and permeameter, respectively. Liquid porosity was measured on saturated samples using a double-weighing on saturated and dried samples, knowing the samples' dimensions. Liquid permeability was measured on saturated samples in an experimental device, knowing the differential pressure and using Darcy's law. The use of different salinities of the saturating brine to measure the sample electrical conductivity enables to determine the formation factor F (–) and the surface conductivity σ_s ($\mathrm{S\,m}^{-1}$), assuming

$$\sigma = \frac{\sigma_w}{F} + \sigma_s, \tag{1}$$

where σ_w ($\mathrm{S\,m}^{-1}$) is the saturating brine conductivity. Note that ~~the~~ surface conductivity can usually be neglected in carbonate material ~~((e.g., Cherubini et al., 2019))~~(e.g., Cherubini et al., 2019). The formation factor is an important parameter that can be related to microstructural properties through appropriate petrophysical relationships (e.g., Rembert et al., 2020). Among

others, it can be related to the porosity of the medium through ~~Archie (1942)~~Archie's equation (1942),

$$F = \phi^{-m_c}, \tag{2}$$

where m_c (–) is the cementation exponent. Many studies use this relationship to find a unique value of m_c to characterize their
90 rock type. From this, for typical carbonate rocks, the cementation exponent is comprised between 2 and 3 (e.g., Lucia, 1983).
However, for highly heterogeneous rocks and samples submitted to dissolution, it has been found that Archie's equation is not
suitable (e.g., Garing et al., 2014; Niu and Zhang, 2019; Revil et al., 2014). Nevertheless, it has been shown that the formation
factor is an interesting proxy to quantify the pore space geometrical properties, such as the tortuosity (e.g., Jougnot et al., 2018).
Clennell (1997) proposes an extensive review of seminal works on tortuosity, among which the model of Winsauer et al. (1952)
95 that describes the electrical tortuosity τ_e (–) as

$$\tau_e = \sqrt{F\phi}. \tag{3}$$

Clennell (1997) also discusses the relationship between electrical and hydraulic tortuosities, τ_h (see also discussions in Thanh
et al., 2019). Recent developments in petrophysics tend to develop physics-based models that rely on more accurate conceptual-
ization of the porous medium geometries ~~(e.g., Rembert et al., 2020; Soldi et al., 2017; Vinogradov et al., 2021)~~(e.g., Rembert et al., 2020;
100 .

In addition, X-Ray MicroTomographic (XRMT) images of the two core samples are collected with a pixel size of 12 μm and
are analyzed with ~~a homemade~~ in-house software to obtain complementary information about the ~~samples structure~~ structure
of the samples. In particular, a pore size distribution is obtained from a probabilistic method displaying the chord lengths.

For further details about rock type, calculation methods and protocols, complete results, and discussion on the ~~samples~~
105 ~~properties~~properties of the samples, the reader will find the information in Leger and Luquot (2021), ~~?, and ?. After dissolution~~
~~, in order~~ Leger et al. (2022b), and Leger et al. (2022a). The same laboratory and imaging characterization was repeated on the
samples after dissolution to estimate the impact of the core-flooding experiments on the ~~core properties, the same laboratory~~
~~and imaging characterization as before the experiments are conducted on the samples~~rock properties.

2.2 Experimental setup and monitoring

110 The experimental protocol followed here is the same as the one used in ~~? and ?~~Leger et al. (2022a) and Leger et al. (2022b)
. Under atmospheric pressure and temperature conditions, an acidic solution is injected through the samples. The injected
solution is composed of water previously balanced with samples of the same rock type mixed with acetic acid (CH_3CO_2H),
and sodium acetate (CH_3CO_2Na). The resulting acid concentration is about 10^{-2} mol L^{-1} buffered with a pH of 4. Figure 1
displays the homemade experimental device used for the percolation experiments.
115 The inlet acid solution is stored in a beaker~~where~~. Its electrical fluid conductivity and pH are monitored continuously ~~,~~
~~and~~ using JUMO sensors and it is injected through the core sample by a peristaltic pump MiniPuls 3 from Gilson, ensuring a
constant flow rate.
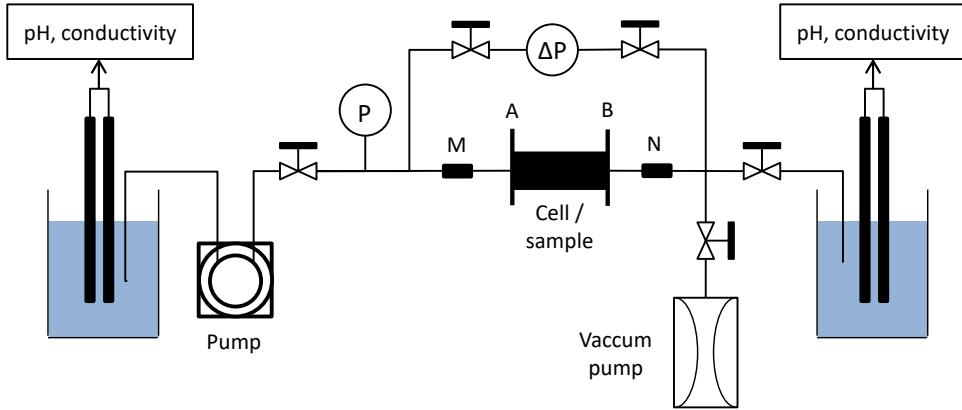
Figure 1. Experimental setup used for the percolation experiments. P is the absolute pressure sensor, ΔP is the differential pressure sensor. A, B, M, and N are the electrodes, with A and B for the electric current injection and M and N for the electric potential measurement.

Sensors Gems and Keller of absolute and differential pressure, respectively, continuously record the pressure difference between the sample inlet and outlet. ~~It allows to calculate~~ This monitoring of the pressure difference allows calculating the evolution of the ~~samples~~ permeability k (m^2) during the experiment using Darcy's law

$$k = \frac{Q\,L\,\mu_w}{A\,\Delta\mathrm{P}}, \tag{4}$$

where Q (m^3 s^{-1}) is the flow rate, L (m) is the sample length, $\mu_w = 0.001$ Pa s is the dynamic viscosity of water, A (m^2) is the area of fluid injection, and ΔP (Pa) is the differential pressure between the inlet and outlet. All of the sensors mentioned above are connected to a Labjack system for continuous acquisition.

~~In order to~~ To evaluate the impact of the hydraulic conditions, E04 and E05 were flushed with two different flow rates, inducing two different transport conditions. These two experiment conditions are associated ~~to~~ with two Péclet numbers ~~Pe~~ Pe (–) defined by

$$\underline{Pe}\text{Pe} = \frac{u\,l}{d}, \tag{5}$$

where u (m s^{-1}) is the flow velocity injected in each sample, ~~$d = 5\,10^{-9}$~~ $d = 5 \times 10^{-9}$ m^2 s^{-1} is the mean value of diffusion coefficients for ions presented in the fluid at $25\,°\mathrm{C}$, and l (m) is the characteristic length, which value is based on the pore size distribution calculated in Leger and Luquot (2021). The corresponding Péclet numbers are ~~$Pe_{E04} = 5.26$ and $Pe_{E05} = 1.97$~~ $\mathrm{Pe}_{E04} = 5.26$ and $\mathrm{Pe}_{E05} = 1.97$. They correspond to flow rates ~~$Q_{E04} = 6.0\,10^{-9}$~~ $Q_{E04} = 6.0 \times 10^{-9}$ m^3 s^{-1} and ~~$Q_{E05} = 2.5\,10^{-9}$~~ $Q_{E05} = 2.5 \times 10^{-9}$ m^3 s^{-1}.

The setup is also equipped with a 4-wire half bridge array to monitor the water-saturated sample electrical resistance R (Ω) with a CR1000 data logger from Campbell Scientific. The measured resistance is converted into the conductivity term $\sigma = 1/(R\,k_g)$, where k_g (m) is the geometrical coefficient determined from the electrodes shape, size, and distance, using 3D

numerical computing on the Electrical Impedance and Diffuse Optical tomography Reconstruction Software (EIDORS). We obtain $k_{g\,E04} = 36$ mm and $k_{g\,E05} = 37$ mm.

At the outlet, fluid samplings of 5 mL are continuously collected during day time and punctually during ~~night time~~ nighttime. pH, brine conductivity, and cation concentrations are measured for each fluid sample. From calcium (Ca^{2+}) concentration monitoring, we can determine the mass of dissolved calcite through time, and thus, obtain the time variations of the rock sample porosity ϕ (–). At time t_i (s) we have $\phi_{t_i} = \phi_{t_{i-1}} + \phi_{dt}$, where ϕ_{dt} (–) is the porosity difference over the time laps $dt = t_i - t_{i-1}$ (s). By definition, $\phi_{dt} = V_{dt}/V_{ech}$, where $V_{ech} = AL$ (m^3) is the core sample volume and V_{dt} (m^3) is the pore volume difference over time laps dt. The latter is calculated as follows

$$V_{dt} = \frac{m_{CaCO_3\,dt}}{\rho_{CaCO_3}} = \frac{([Ca^{2+}]_{t_i} - [Ca^{2+}]_{t_0})\,dt\,Q\,M_{CaCO_3}}{\rho_{CaCO_3}}, \tag{6}$$

where $m_{CaCO_3\,dt}$ (g) is the mass of calcium carbonate over time laps dt, ρ_{CaCO_3} (g m^{-3}) is the density of calcium carbonate, $[Ca^{2+}]_{t_i}$ (mol m^{-3}) is the calcium concentration at the sampling time t_i, $[Ca^{2+}]_{t_0}$ (mol m^{-3}) is the initial calcium concentration, and M_{CaCO_3} (g mol^{-1}) is the molecular ~~masses~~ mass of calcium carbonate.

2.3 Analytical model

2.3.1 Capillary Size Distribution

To relate the electrical monitoring with the porous medium microstructure, we use the Bundle Of Capillary Tubes (BOCT) approach (e.g., Vinogradov et al., 2021). It uses a bundle of parallel tortuous and constrictive capillaries as a conceptualization of the pore structure (e.g., Guarracino et al., 2014; Rembert et al., 2020). The conceptual geometry is represented in Fig. 2.
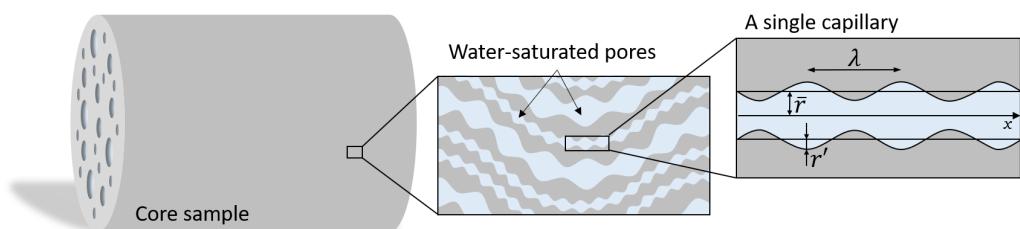
Figure 2. The porous rock model is composed of a large number of sinusoidal and tortuous capillaries in the cylindrical Representative Elementary Volume (REV) corresponding to the core sample. All the capillaries have the same tortuous length and their radii follow a fractal distribution. The considered pore geometry corresponds to the one from ~~Guarracino et al. (2014)~~ Guarracino et al. (2014): $\bar{r}$ is the average pore radius while r' is the amplitude of the sinusoidal fluctuation, and λ is the wavelength.

The BOCT model considers N capillaries that do not intersect and run with the same orientation. The capillaries are confined within a cylindrical model of length L (m) and radius R (m). They are permitted to have different radius r (m), but a single length l. Thus, the tortuosity $\tau = l/L$ (–) is an effective property. Each tortuous and constrictive capillary presents a varying radius $r(x)$ (m) defined with the following sinusoidal expression,

$$r(x) = \bar{r} + r' \sin\left(\frac{2\pi}{\lambda}x\right) = \bar{r}\left(1 + 2a \sin\left(\frac{2\pi}{\lambda}x\right)\right),$$ (7)

where $\bar{r}$ (m) is the average capillary radius, r' (m) the amplitude of the radius size fluctuation, and λ (m) the wavelength. The parameter a (–) is the pore radius fluctuation ratio, also called the constriction factor. It is defined by $a = r'/2\bar{r}$, thus ranging from 0 to 0.5, corresponding to cylindrical pores ($r(x) = \bar{r}$) and periodically closed pores, respectively.

From Jackson's formulation based on capillary radius (Jackson, 2008), the number of capillaries is expressed as

$$N = \int_{\bar{r}_{min}}^{\bar{r}_{max}} n(\bar{r})d\bar{r},$$ (8)

with $n(\bar{r})d\bar{r}$ the number of capillaries of radius between $\bar{r}$ and $\bar{r} + d\bar{r}$. As many geologic materials present a skewed pore size distribution (e.g., Bennion and Griffiths, 1966; Dullien, 1992), we use a pseudo-fractal law to describe the distribution of capillaries throughout the model (Jackson, 2008; Vinogradov et al., 2021)

$$-dN = n(\bar{r})d\bar{r} = D\left(\frac{\bar{r} - \bar{r}_{max}}{\bar{r}_{min} - \bar{r}_{max}}\right)^{m_j},$$ (9)

where $0 < m_j < \infty$ is a dimensionless exponent. $\bar{r}_{min}$ and $\bar{r}_{max}$ (m) are the extreme average pore sizes. They are estimated from the chord length computation using 3D tomography of the samples before and after the dissolution experiments. Thus, N is calculated for average pore sizes $\bar{r}$ comprised between these two extremes. The normalization coefficient $D = 1$ since the pore size distribution from the chord lengths estimation is normalized and expressed in percent. The minus sign of $-dN$ implies that the number of pores decreases when the average radius increases (Soldi et al., 2017; Thanh et al., 2019; Yu et al., 2003).

2.3.2 Electrical properties

We follow the approach of Rembert et al. (2020), which consists of the expression of the electrical properties at the pore scale before upscaling them considering the bundle of capillaries as an equivalent circuit of parallel conductances. This approach is valid for negligible surface conductivity and leads to

$$\sigma = \frac{\sigma_w \phi (1 - 4a^2)^{3/2}}{\tau^2 (1 + 2a^2)} = \frac{\sigma_w \phi f}{\tau^2},$$ (10)

where f (–) is the constrictivity of the porous medium varying from 0 to 1, corresponding to periodically closed capillaries and cylindrical capillaries, respectively. This approach quantifies the effect of pore throats and pore bodies on the medium electrical conductivity.

~~Neglecting the surface conductivity in~~ Eq. ~~, Eq.~~ (10) leads to the following definition of the formation factor

$$F = \frac{\tau^2}{\phi f}. \tag{11}$$

Rembert et al. (2020) demonstrated that the constriction factor and the tortuosity vary during ~~dissolution process,~~ the dissolution process since it affects the structure of the porous medium. Thus, $a(\phi)$ and $\tau(\phi)$ are defined following logarithmic laws

$$a(\phi) = -P_a \log(\phi) \tag{12}$$

and

$$\tau(\phi) = 1 - P_\tau \log(\phi), \tag{13}$$

where P_a and P_τ are empirical dimensionless parameters.

2.3.3 Johnson length

The Johnson length Λ (m) represents a characteristic length that corresponds to the dynamically connected pores (Banavar and Schwartz, 1987; Ghanbarian, 2020). Following Johnson et al. (1986), it can be defined from the permeability and the formation factor ~~by~~ as

$$\Lambda = \sqrt{8kF}. \tag{14}$$

Numerical studies have shown that calcite dissolution can strongly modify this characteristic length Λ (Niu and Zhang, 2019).

3 Results and Discussion

3.1 Hydro-chemical and electrical results from percolation experiments

Figure 3 displays the evolution over time of measured and calculated parameters for the two percolation experiments, with red curves for E04 and blue curves for E05. In detail, there are porosity, permeability, outlet pH values, calcium concentration and core sample conductivity, water conductivity, and normalized formation factor. The initial and final values of the measured parameters obtained from petrophysical measurements are presented in Table 1. They are also represented for the initial and final porosity with error bars, permeability, and normalized formation factor values as diamonds and circles for E04 and E05, in Fig. 3, respectively. One can note that error bars are higher for final porosity values compared to the initial values. This comes from the formation of conduits through the sample due to dissolution, which allows water to leak out and is responsible for the measurement accuracy deterioration. The normalized formation factor, presented in Fig. 3f, comes from the normalization with the first value of the apparent formation factor, itself calculated using the outlet values of the pore water conductivity. The normalized formation factor is used to propose a fair comparison with the difference between the initial and final values of the formation factor obtained from petrophysical characterization.
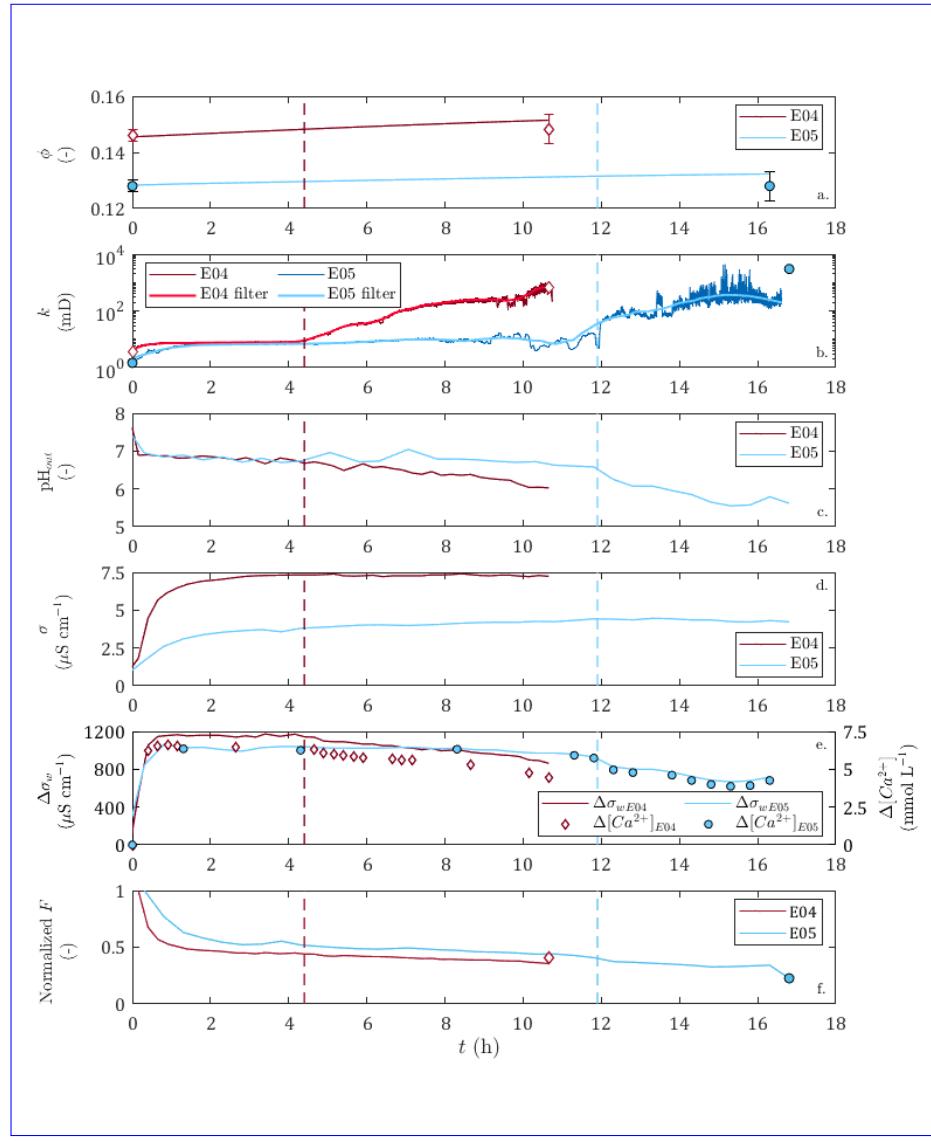
Figure 3. Time variations for E04 and E05 dissolution experiments of (a) the porosity, (b) the permeability, (c) the pH of the outlet sampled solution, (d) the ~~differential calcium concentration between the inlet solution and the sampled outlet solution, and the~~ rock sample electrical conductivity, (e) the differential electrical conductivity (lines) and calcium concentration (diamonds and disks) between the inlet solution and the sampled outlet solution, and (f) the normalized formation factor. The red and blue vertical dashed lines correspond to the percolation times of E04 and E05, respectively. Apart from calcium data points, diamonds and circles represent the initial and final porosity with error bars, initial and final permeability, and normalized final formation factor values obtained from petrophysical measurements for E04 and E05, respectively.

Table 1. Petrophysical properties from laboratory measurements of samples at initial and final states, i.e., before and after the percolation experiments with porosity ϕ_L (%), permeability k_L (mD), formation factor F_L (–), cementation exponent m_L (–) and electrical tortuosity τ_e (–). The index L stands for Laboratory measurements and ϕ_{ch} (–) is the porosity from chemistry calculations.

	Samples	ϕ_L		k_L	F_L	m_L	τ_e
Initial	E04	14.6		3.77	103.1	2.41	3.87
	E05	12.8		1.47	222.2	2.63	5.34
	Samples	ϕ_L	ϕ_{ch}	k_L	F_L	m_L	τ_e
Final	E04	14.8	15.1	700	41.5	1.95	2.48
	E05	12.8	13.2	3000	50.3	1.90	2.53

One can observe that E04 and E05 curves present similar amplitudes and shapes for all the measured and calculated parameters displayed in Fig. 3. However, due to lower flow regime (?)(Leger et al., 2022a), the curves of E05 present retarded or lower variations compared to E04 curves.

The generation of dissolved calcium (Fig. 3de) and the increase of porosity (Fig. 3a), permeability (Fig. 3b), and water conductivity difference (Fig. 3e) indicate that calcite dissolution is the main chemical reaction for both experiments. However, calcium difference shows a slow decrease until the end of the experiment, which can also be seen in the pH curves and the water conductivity difference curves (Fig. 3c and e), and indicates that the dissolution regime was initially strong and got weaker over time.

The permeability curves of both samples (Fig. 3b) show a small initial increase followed by a stabilization for a few hours, then they increase sharply and reach final values several orders of magnitude higher than the initial values. The initiation of this sharp increase in permeability is interpreted as being due to the breakthrough of the sample by the acid solution, and the corresponding time, defined as the percolation time, is highlighted as a vertical dashed line in Fig. 3 (in red for E04 and blue for E05). Since the acquisition rate is high compared to time variations before percolation, we estimate the standard error around 10^{-2} mD over this range. The percolation times are 4.3 and 11.9 h for E04 and E05, respectively. For E05, the percolation time is also observable through a slight break in slope on the pH, dissolved calcium, and water conductivity curves.

Before the percolation time, one can observe that the E05 permeability curve presents variations attributed to complex effects of grain displacement and transitory pore clogging. After percolation time, both E04 and E05 permeability curves present high-frequency noise corresponding to the limit of detection of the sensors of differential pressure. In order to To avoid these instabilities, the curves are filtered. After a comparison with the moving average and Butterworth filters, we choose the Savitsky-Golay filter, since it offers a better adjustment. We observe that the filtered curves are well superimposed on the curves of the measurements, except between 10 and 12 h for the dissolution of E05, because of the transient complex effects. The final permeability of E05 is higher than the last value of the temporal series. This discrepancy is also due to the limit of detection of the sensors of differential pressure. However, we did not take this higher value into account when filtering, to be in accordance with the temporal series.

The sample conductivity increases during both experiments (Fig. 3d). At first glance, this increase could be attributed to the increase of the pore water conductivity (Fig. 3e) instead of calcite dissolution. However, one can observe that the nor-
235 malized formation factor (Fig. 3f) decreases during the experiment. Thus, the sample conductivity and formation factor variations are linked to calcite dissolution. It can be observed that for sample conductivity and formation factor, the variations are monotonous, with a rapid initial change followed by a gentler slope until the end of the experiment. The initial slopes are correlated to higher calcium concentrations at the beginning of the experiment (Fig. 3~~d~~e) and are, thus, due to initial strong dissolution regimes. The sample conductivity and formation factor smooth variations show that they are more impacted by
240 porosity increase than by permeability variations (Fig. 3a and b). Over this time range, the acquisition rate of the sample conductivity is high compared to the time variations. We estimate the standard error around 10^{-3} μS m^{-1}. Furthermore, the comparison of the results between E04 and E05 shows that with equal water conductivity and close permeability values before the breakthrough, higher porosity induces higher sample conductivity. Compared to the petrophysical measurements, the normalized formation factor curves show good agreement with the measured amplitude difference between the initial and final
245 values~~and~~, represented as the final normalized formation factor (Fig. 3f).

3.2 Applying the pseudo-fractal law to the chord length distribution

~~?~~ The analytical model for structural interpretation of the electrical conductivity measurement is based on the pseudo-fractal law developed in Jackson (2008), describing the frequency distribution of capillary size using Eq. (9). In this section, to asses of the model validity on the studied rock samples, we compare the proposed analytical solution for the capillary size distribution
250 with the chord length distribution, a statistical correlation function developed in the study of Torquato and Lu (1993) and derived from the micro CT images of the rock samples published in Leger and Luquot (2021).

For the study of porous media, the chord length distribution corresponds to the probability of finding a line segment wholly in the pore space when randomly thrown into the sample. Leger and Luquot (2021) have published the chord length distribution of E04 and E05 samples before and after percolation in X, Y, and Z directions. Since ~~there are some slight variations depending~~
255 slight variations depend on the direction, we ~~apply the pseudo-fractal law describing the distribution of capillaries using Eq. on the~~ consider the mean chord length distribution. The adjusted parameter m_j, defined above, is determined using a Monte-Carlo optimization scheme. From the results displayed in Fig. 4, the pseudo-fractal law shows a good agreement with the chord length distributions for both samples. This result is a major validation of the hypothesis on which the model is based and guarantees the reliability of the following interpretation of the model's results.
260 ~~In order to attest of~~ To attest to the accuracy of the pseudo-fractal law to describe the chord length distribution, we computed the corresponding error $\epsilon < 0.5\,\%$ for each value of the exponent m_j. The error ϵ is defined as follows

$$\epsilon = \frac{1}{N^d} \sum_{i=1}^{N^d} |n_i^d - n_i^m|, \tag{15}$$

where N^d, n_i^d, and n_i^m refer to the number of data, the number of capillaries from the data, and the number of capillaries from the model, respectively. The best adjustment is found for values of m_j of the same order of magnitude (see legends of
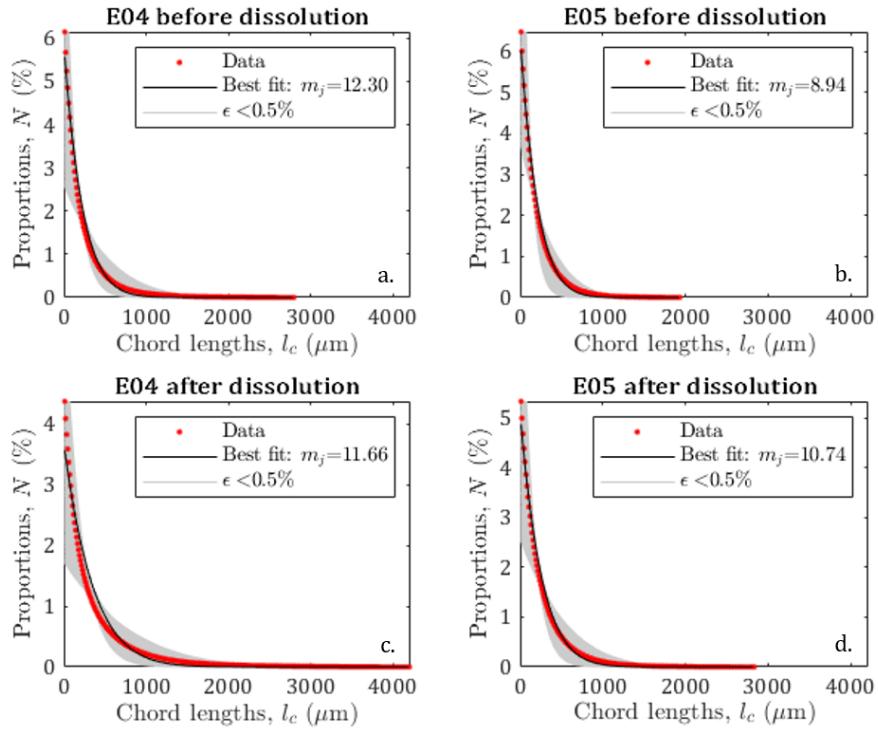
Figure 4. Pore size distribution of E04 and E05 core samples before and after dissolution from the chord length estimation (red curve), from the pseudo-fractal law (black curve corresponds to the best adjustment of the power law exponent and gray curves correspond to the pseudo-fractal fit with an error of less than 0.5%.

265   Fig. 4), reflecting that E04 and E05 are samples of the same rock type. However, since m_j can vary over large ranges, the slight differences obtained for the four different data sets (although accurately determined, see Appendix A), cannot be interpreted as the impact of the dissolution on this parameter describing the pore size distribution, while percolation has a huge impact on the rock properties as presented above (see Fig. 3 and Table 1). Thus, the evolution of m_j ~~is not a sufficient indicator of~~ shows that the effect of dissolution on the sample ~~.~~ has no important effect on the capillary size distribution. This result is not surprising

270   since given the observation made by Leger et al. (2022a) about the dissolution pattern for E04 and E05. Indeed, from micro CT images, both samples present a wormhole-dominant dissolution regime, meaning that the acid percolation is focused on main paths and does not alter the entire pore volume.

     Moreover, ~~?~~ Leger et al. (2022a) have also determined the pore size distribution by centrifugation. Since the size intervals for the determination of the pore number are not regular, we could not use the pseudo-fractal law on these data. Nevertheless,

275   the characterization of pore size distribution by centrifugation has shown that between 46 and 70 % of the pores have a pore size comprised between 0.5 and 12 μm, while the minimal resolution of the chord length is of 12 μm. In addition, a very

porous area of the sample only composed of small pores can be interpreted by the tomography software as a single pore over the entire pixel. This means that the chord length distribution ~~has not~~ does not have the best precision for the ~~smallest pores distribution~~distribution of the smallest pores. However, Leger and Luquot (2021) noticed the pore size distribution from the two methods ~~are~~ is similar and consistent ~~, leading to the conclusion that large pores are more likely to control rock parameters on core scale. In addition, this importance of macropores is even more of interest in reactive transport, as it can be seen in fractured media (e.g., Noiriel, 2015; Garcia-Rios et al., 2017)~~on comparable pore size ranges. This observation underlines the interest in using a fractal model for this study since the tendency of the fractal law to impose a majority proportion of small pores coincides with the estimate of the pore size distribution obtained by centrifugation.

3.3 Influence of rock structure on electrical signature~~:~~: the major role of constrictivity

We have shown in the previous section that the pore size distributions of both samples were successfully describable using pseudo-fractal laws. Thus, we can apply the relationship relating the formation factor and the porosity developed in Eq. (11). We can see in Fig. 5 the results of the Monte-Carlo inversions to adjust the constrictivity f, defined from Eq. (10), and the tortuosity τ. To reflect the structural changes in the porous medium, we consider the parameters as distributions $a(\phi)$ and $\tau(\phi)$, expressed in Eq. (12) and Eq. (13). We observe that the evolution of f and τ with the porosity is physically plausible as the increase of porosity due to calcite dissolution reflects less complex medium geometries (i.e., less constrictive and less tortuous), described with higher values of f and lower values of τ. The accuracy of the model is evaluated using the error computation of Eq. (15). ~~For both samples it is~~ Both samples are below 10 %.

The constrictivity varies over different ranges of values between E04 and E05 (Fig. 5c and d). For E05, f is lower by half (i.e., more constrictive) compared to E04, which is in agreement with E04 higher porosity values. In contrast, the evolution with porosity follows roughly the same law for these two samples. This indicates that we are working on two samples of the same rock type with similar pore shapes.

The tortuosity varies little during the experiment for both samples, although it is more pronounced for E05 (Fig. 5e and f). A surprising result is that the tortuosity values are higher for E04 than for E05, while E05 is less porous. This result is in contradiction with the values of initial and final electrical tortuosity τ_e displayed in Table 1, showing higher values for both samples and higher values for E05 compared to E04. This discrepancy has already been observed in Niu and Zhang (2019) and can be explained with the definition of τ_e, given in Eq. (3), which combines the impact of the tortuosity and the constrictivity and is, thus, artificially higher. Moreover, the main ~~conduits~~ paths generated by dissolution can be visualized from tomographic images. Figure 6 shows for the two samples the phase formed by dissolution that connects the ~~phase connecting the~~ inlet to the outlet~~for the two samples~~, according to two different image treatments. ~~Two segmentations based on a region growing method were~~ This procedure does not allow discretizing the pore space in terms of quantified pore sizes since it is based on grayscale visualization and segregation: it is a qualitative procedure. The two segmentations applied to isolate two different void phases are based on a region-growing method. The red phase represents the phase connecting the largest pores in the samples from the inlet to the outlet, as already explained and used in ~~?~~Leger et al. (2022a). The blue phase only shows the darker pixels of the images, corresponding to the center of the conduit used by the fluid to cross the samples. In comparison, E05 has a straighter
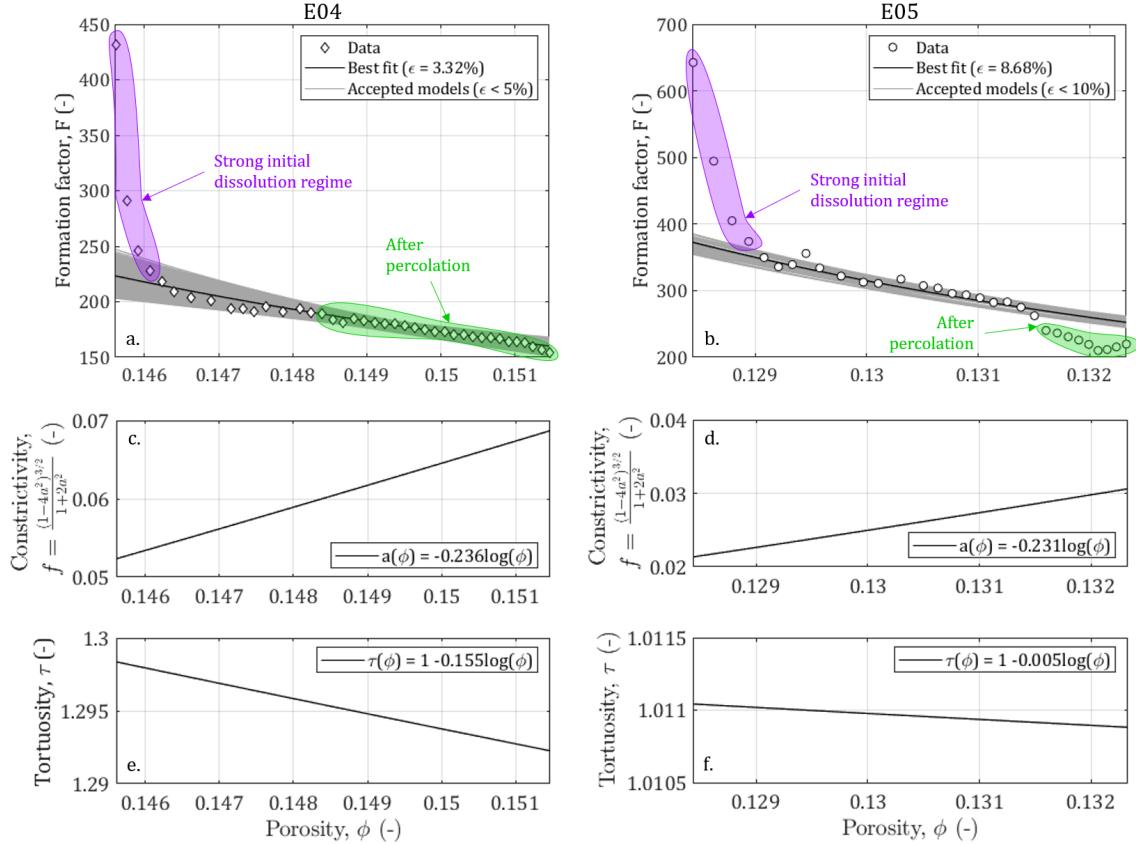
Figure 5. Results of the Monte-Carlo modeling of the relationship between the formation factor and the porosity for samples E04 and E05 affected by calcite dissolution and evolution of the constrictivity and the tortuosity in function of the porosity increase.

path than E04. Thus, the model parameters adjustment reproduces well the tomography observations and the experimental electrical data.

However, for the lowest porosity data in Fig. 5, the formation factor shows high values, highlighted in purple, that do not fit with the gentle slope of the model. As mentioned earlier, these points correspond to an initial strong dissolution regime that is out of the validity domain of the model (Guarracino et al., 2014; Rembert et al., 2020). Moreover, the points in green in Fig. 5 highlight the data acquired after the percolation, where the samples cannot be considered anymore as representative elementary volume (REV) and where the model is not valid ~~neither~~ either. Nevertheless, for E04, the acid percolation does not show radical changes in the formation factor and porosity ~~compare~~ compared to the smooth tendency that follows the initial strong dissolution regime, whereas, for E05, the formation factor falls out of range after percolation. These different behaviors are due to the imposed hydrodynamic regimes and their consequences on the dissolution profile. Indeed, the red phase in Fig. 6 shows that the new paths created in E04 are concentrated in a reduced volume of the sample, while for E05 the red phase
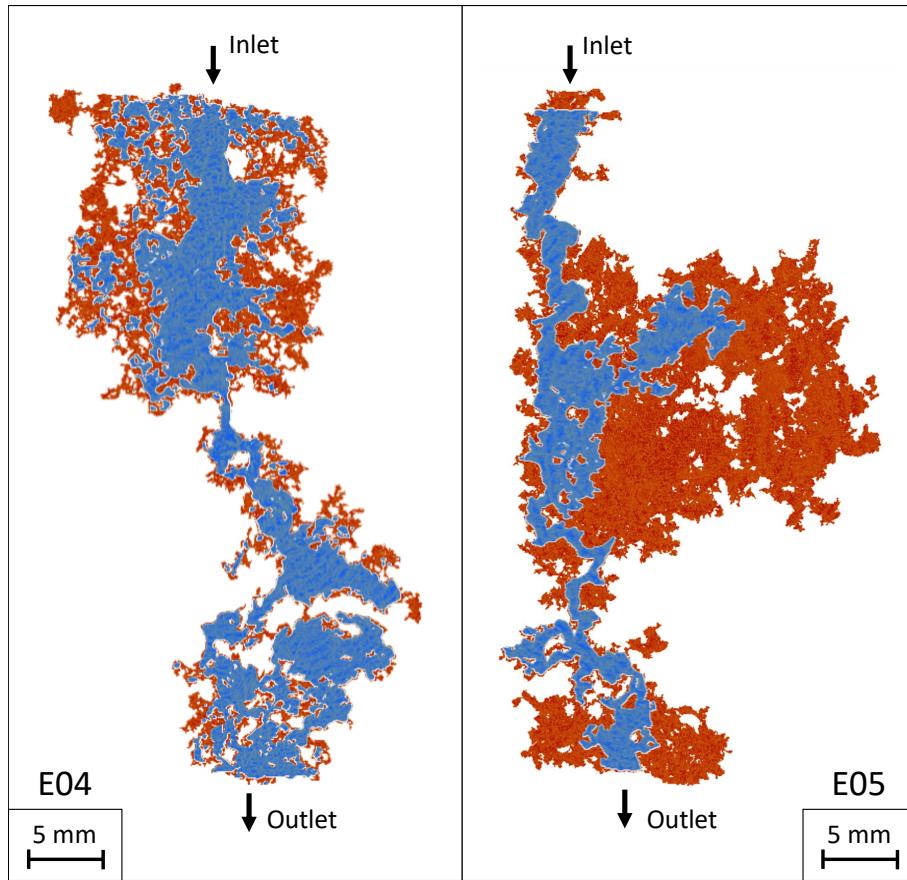
Figure 6. Main path conduits of E04 and E05 opened due to calcite dissolution. The samples are displayed with the acid injection from the top to the bottom. The red phase shows the complete connected phase and the blue phase shows a restricted phase where the flow concentrates.

is extensively spread in the upper part of the sample. This portion of the sample, close to the inlet, was probably dissolved at an early stage of the experiment, therefore, creating no apparent effect on the permeability or formation factor before the sample percolation. E04 and E05 are dissolved with Péclet numbers different but of the same order of magnitude. One could

325   expect similar flow conditions and flow patterns. However, regarding the paths created in both samples in Fig. 6, Micro CT images show that this difference in flow regime already has an impact on the dissolution pattern. Indeed, even if both samples end up with the formation of a dominant conduit, E05 presents a peripheric portion invaded by the acid solution and which has an important impact on the electrical conductivity due to a percolation time happening almost three times more than the percolation time of E04.

330

3.4 Influence of hydrodynamic properties on rock structure and electrical signature

3.4.1 Impact of the experimental conditions and permeability changes

In this section, we ~~are interested in highlighting~~ focus on the link between the evolution of hydrodynamic and electrical properties. The permeability is plotted as a function of the formation factor and porosity in Fig. 7. We can first note that the permeability varies over the same ranges of values for both samples, while E04 has a larger porosity (and lower formation factor) compared to E05. As discussed in the literature (e.g., Guarracino et al., 2014; Soldi et al., 2017; Rembert et al., 2020), the pore throats play a primary role ~~on~~ in the hydrodynamic behavior of porous media. According to the model used in this study, the studied samples follow the same distribution for constrictivity (Fig. 5), which is consistent with the similarity in permeability.
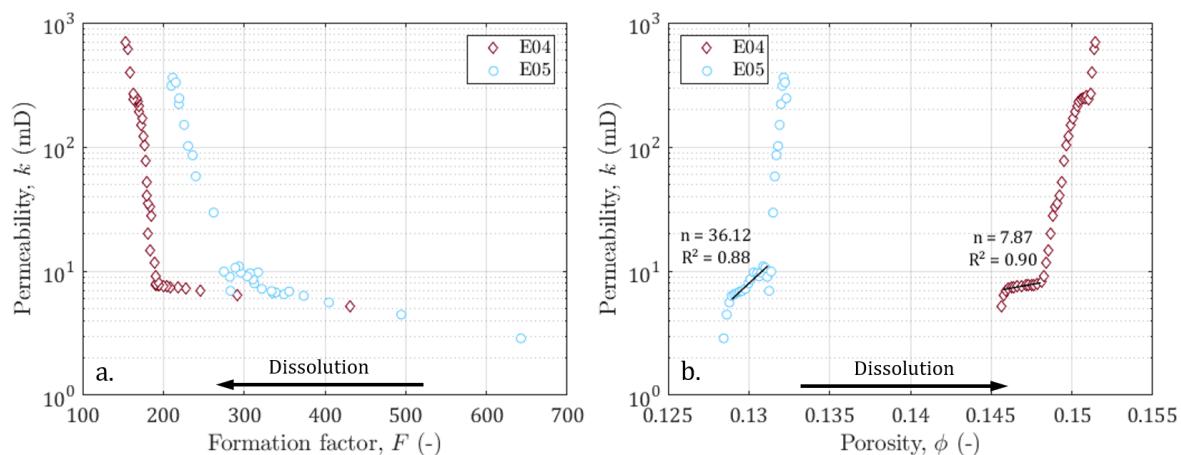
Figure 7. Permeability against (a) formation factor and (b) porosity. Black arrows indicate the direction of the impact of dissolution on the formation factor and porosity. Black lines and annotations indicate the slopes, the exponent, and the coefficient of determination of the Kozeny-Carman equation for the data before percolation.

It can be observed that before the breakthrough, the permeability increases little, while the formation factor and the porosity vary strongly. Then, after percolation, the trends are reversed, and the permeability increases strongly compared to the lower variation of the porosity and the formation factor. This behavior change is very clear for both samples and indicates that monitoring electrical properties allows us to be sensitive to the impact of dissolution on the porous medium long before the sample is percolated.

~~In order to locate our experiments in the scientific landscape~~To compare our results with previously published data, we plotted our data with the well-known power-law relating permeability and porosity $k \sim \phi^n$ (Kozeny, 1927; Carman, 1937), where n (–) is an empirical exponent. This relationship has been widely used in literature, sometimes by trying to determine the n exponent (Martys et al., 1994), sometimes by taking into account the critical pore size (Gueguen and Dienes,

1989; Thompson et al., 1987), the specific surface with the Kozeny factor (Paterson, 1983; Walsh and Brace, 1984; Fabricius
et al., 2007; Weger et al., 2009), or the grain diameter in a non-fractal (Kozeny, 1927; Carman, 1937, 1948, 1956; Bourbie
et al., 1987) or in a fractal dimension (Pape et al., 1999; Costa, 2006). The classic ~~power-law~~ power law has been tested
here and the n values obtained are ~~a bit high , but are still~~ high compared to the value $n = 3$ found for granular packings in
constant structure formation (Kozeny, 1927) but are consistent with those proposed in the literature on ~~carbonate rocks, known
for their natural heterogeneity and also the one created by dissolution (see **?**, for a synthetic review)~~limestone dissolution
(e.g., Noiriel et al., 2004, 2005; Menke et al., 2015, 2016), due to the heterogeneity created by the chemical reaction (see Leger et al., 2022)
.

3.4.2 The characteristic pore size defined through the Johnson length

The comparison of the permeability of E04 and E05 reveals that they are samples with similar initial hydrodynamic properties
related to their identical rock type (Table 1). However, their difference ~~of~~ in porosity leads to different ranges for the formation
factor, and the different imposed hydrodynamic regimes lead to higher final permeability for E05. Moreover, ~~the use of~~ using
a normalized formation factor (Fig. 3~~) enables to compare~~ f) enables comparing trends but does not allow ~~to quantitatively
interpret~~ quantitative interpretation of the electrical monitoring in ~~term~~ terms of rock structure. Thus, as recommended by Niu
and Zhang (2019), we use the Johnson length as an effective pore size (Fig. 8), that enables ~~to compare~~ comparing the behavior
of both samples E04 and E05 regarding other data sets from the literature (Niu and Zhang, 2019; Vialle et al., 2014).
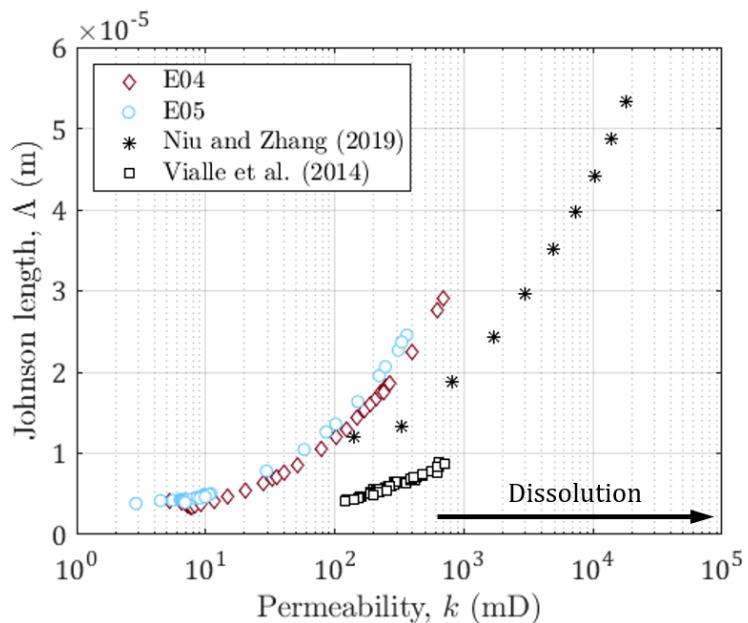
Figure 8. Johnson length against the permeability for E04, E05, and data sets from Niu and Zhang (2019) and Vialle et al. (2014). The black
arrow indicates the direction of the impact of dissolution on the permeability.

The series from Niu and Zhang (2019) comes from calcite dissolution simulation of a digital image of a carbonate mudstone (Wellington Formation, Kansas, USA), that has an initial porosity of 0.13. The fluid transport is assumed as advection dominated (~~$Pe > 1$~~$Pe > 1$), and under this transport condition, referring to Pereira Nunes et al. (2016), they impose a transport-limited case, related to ~~wormholing~~conduit formation, in which the reaction at the solid-liquid interface is limited by the diffusion of reactants to and from solid surfaces (~~$PeDa > 1$, where $Da = k_r/u$~~$PeDa > 1$, where $Da = k_r/u$ is the so-called Damköhler number, and k_r is the local reaction rate).

The data points from Vialle et al. (2014) correspond to bioclastic limestone (Estaillades limestone, France), composed of more than 99% calcite, and of initial porosity of 0.29. The values for ~~Pe ranges~~Pe range from 18.5 (for the smaller grains) to 37 (for the larger ones) and ~~$Da = 3486$~~$Da = 3486$. Meaning that for this data set, the dissolution is also transport controlled and leads to dominant wormhole formation.

~~One can observe that all the~~For E04 and E05, with the formula from Menke et al. (2015) the authors calculate $Da_{E04} = 4.1 \times 10^{-5}$ and $Da_{E05} = 8.9 \times 10^{-5}$. These low Damköhler values should lead to uniform dissolution, as established by Golfier et al. (2002) in their diagram. However, this result does not stand with the micro CT images. As discussed in Menke et al. (2016) and Leger et al. (2022b), the threshold values proposed in the diagram published in Golfier et al. (2002) are not applicable for heterogeneous porous media. Indeed, the rock initial heterogeneities allow for preferential paths which channel the reacting solution and lead to a dominant wormhole dissolution regime.

All the series present the same behavior, but with different trends and on different ranges. These differences do not seem related to the initial porosity value~~or hydrodynamic regime~~, hydrodynamic regime, and dissolution pattern. Indeed, for different Péclet numbers, there are close values and trends for E04 and E05 compared to the other series. In addition, while the carbonate mudstone from Niu and Zhang (2019) presents a similar initial porosity value with E05, ~~they~~these samples do present contrasted Johnson lengths. Moreover, from Damköhler and Péclet numbers and micro CT observations, all of these series fall within the dominant wormhole dissolution regime. Thus, the Johnson length is related to the rock type and highlights the difference in the pore structure among the samples.

4 Conclusions

This study investigates the impact of calcite dissolution on the sample electrical conductivity monitoring through percolation experiments of two crinoidal limestone core samples in different hydrodynamic conditions ~~. We, thus, demonstrate that lower the Peclet condition applied to the samples is, lower the dissolution rate is.~~and analytical modeling of the sample electrical conductivity based on the structural description of the samples.

We first demonstrate that the pore size distribution of these two samples can be approximated by a fractal distribution according to the statistical analysis of micro CT images and centrifugation results. This validation allows for the upscaling procedure of the sample electrical conductivity model to be used in the conceptualization of the samples as bundles of capillaries.

Then, according to the model description, we express the sample electrical conductivity and the formation factor in terms of effective petrophysical parameters: tortuosity and constrictivity. In this representation, the pore space is conceptualized as a fractal cumulative distribution of tortuous capillaries with a sinusoidal variation of their radius (i.e., periodic pore throats). The confrontation of the model with the formation factor versus porosity monitoring for both samples shows that the model can reproduce structural changes linked to calcite dissolution. We observe that dissolution leads to a less constrictive rather than less tortuous sample, thus, designating constrictivity as a property of the pore structure that is impacted by dissolution processes to a greater extent, while most of the literature focuses on the tortuosity and even neglects this parameter when describing the pore space complexity with electrical conductivity measurements.

In addition, we confront the formation factor variations to the evolution of permeability with time. We show that monitoring electrical properties allows us to sense the impact of dissolution in the porous medium long before the sample is percolated. This result is a key finding to highlight the great interest that electrical properties can represent in monitoring reactive percolation in karst systems. Moreover, the obtained results show that the electrical response presents an averaged behavior, which does not allow us to describe the high-frequency variations observed in the permeability data. These instabilities seem to be related to fleeting microscopic processes that could be investigated at smaller scales.

We also link the formation factor to permeability through the characteristic Johnson length. We show on the experimental data of this study and other data sets (experimental and numerical) from the literature on carbonate dissolution that the Johnson length is a relevant parameter that allows comparison of dissolution impact on the pore structure in comparable Péclet-Damköhler conditions (i.e., dominant wormhole) on different rock types (crinoidal limestone, carbonate mudstone, and bioclastic limestone).

We believe that the present study expands our understanding of the links between the electrical conductivity measurement and the evolution of the hydrodynamic and structural properties of the porous medium subjected to dissolution. Nevertheless, the hydrodynamic range of this study was limited and multiple other reactive transport scenarios can be investigated.

Data availability. The data used in this study are available in the Zenodo repository (https://zenodo.org/record/6908522).

Sample availability. Samples of the same rock type are available upon request.

Appendix A: Accuracy of the determination of the pseudo-fractal exponent

The accuracy of the pseudo-fractal computation for the determination of the pore size distribution is controlled through the error ϵ defined in Eq. (15). Since dissolution does not generate notable variations of the pseudo-fractal exponent m_j, we confront the computed error to a range of value m_j in Fig. A1. We obtain V-shaped curves for each data set, showing that m_j is well-determined for each sample, before and after percolation experiments.
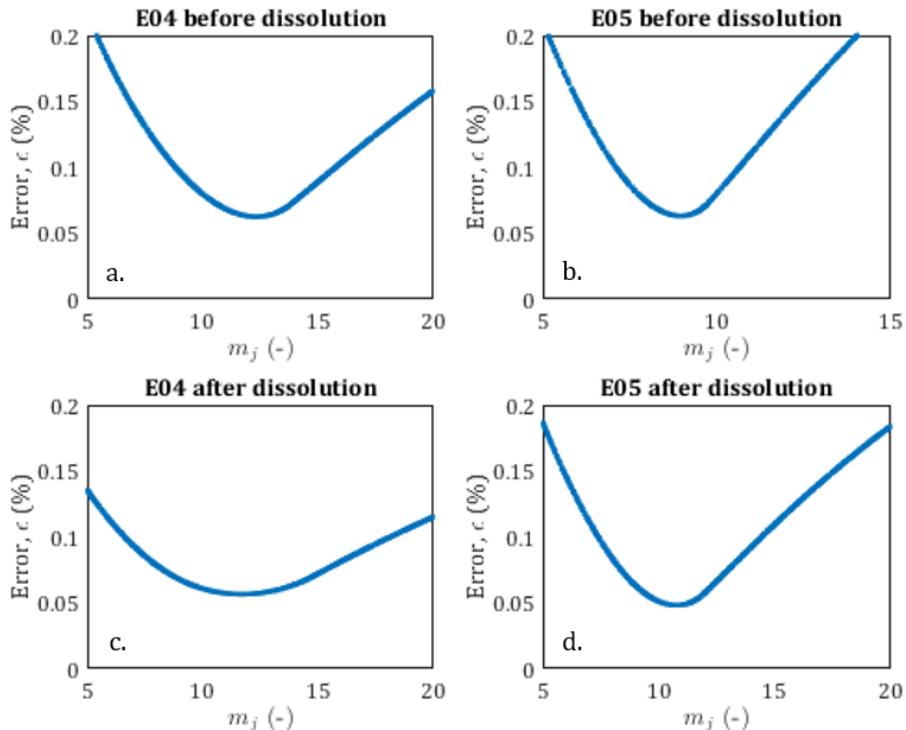
Figure A1. The error of the pseudo-fractal law against the exponent m_j.

Author contributions. Conceptualization, F.R., M.L., D.J., and L.L.; Data curation, F.R. and M.L.; Formal Analysis, F.R., Funding acquisition, F.R. and L.L.; Investigation, M.L.; Methodology, F.R., M.L., D.J., and L.L.; Project administration, L.L.; Resources, D.J. and L.L.; Software, F.R., M.L., and D.J.; Supervision, D.J. and L.L.; Validation, M.L.; Visualization, F.R. and M.L.; Writing – original draft, F.R.; Writing – review & editing, F.R., M.L., D.J., and L.L.

Competing interests. No competing interests are present.

Acknowledgements. This research was funded by the research projects EC2CO (CNRS-INSU) StarTrek and JPI-Water UrbanWat from WaterWorks2017, by the LabEx VOLTAIRE (ANR-10-LABX-100-01), and by a CIFRE PhD fellowship provided by Voxaya and ANRT. We acknowledge the MRI platform member of the national infrastructure France-BioImaging supported by the French National Research Agency (ANR-10-INBS-04, "Investments for the future"), the labex CEMEB (ANR-10-LABX-0004) and NUMEV (ANR-10-LABX-0020). We also acknowledge the petrophysics plateform members of Geosciences Montpellier Laboratory.

440

References

Archie, G. E.: The electrical resistivity log as an aid in determining some reservoir characteristics, Transactions of the AIME, 146, 54–62, https://doi.org/10.2118/942054-G, 1942.

445 Bakalowicz, M.: Karst groundwater: a challenge for new resources, Hydrogeology journal, 13, 148–160, https://doi.org/10.1007/s10040-004-0402-9, 2005.

Banavar, J. and Schwartz, L.: Magnetic resonance as a probe of permeability in porous media, Physical Review Letters, 58, 1411—-1414, https://doi.org/10.1103/PhysRevLett.58.1411, 1987.

Ben Moshe, S., Kessouri, P., Erlich, D., and Furman, A.: Geophysically based analysis of breakthrough curves and ion exchange processes
450 in soil, Hydrology and Earth System Sciences, 25, 3041–3052, https://doi.org/10.5194/hess-25-3041-2021, 2021.

Bennion, D. and Griffiths, J.: A stochastic model for predicting variations in reservoir rock properties, Society of Petroleum Engineers Journal, 6, 9–16, https://doi.org/10.2118/1187-PA, 1966.

Binley, A. and Kemna, A.: DC resistivity and induced polarization methods, Springer, Y. Rubin and S. S. Hubbard (eds.), Hydrogeophysics, https://doi.org/10.1016/B978-0-444-53802-4.00188-3, 2005.

455 Binley, A., Hubbard, A. S., Huisman, J. A., Revil, A., Robinson, D. A., Singha, K., and Slater, L. D.: The emergence of hydro-geophysics for improved understanding of subsurface processes over multiple scales, Water Resources Research, 51, 3837–3866, https://doi.org/10.1002/2015WR017016, 2015.

Bourbie, T., Coussy, O., and Zinszner, B.: Acoustics of Porous Media, Acoustical Society of America, Houston, TX, gulf publishing company edn., 1987.

460 Buckerfield, S. J., Quilliam, R. S., Bussiere, L., Waldron, S., Naylor, L. A., Li, S., and Oliver, D. M.: Chronic urban hotspots and agricultural drainage drive microbial pollution of karst water resources in rural developing regions, Science of The Total Environment, 744, 140 898, https://doi.org/10.1016/j.scitotenv.2020.140898, 2020.

Burchette, T. P.: Carbonate rocks and petroleum reservoirs: a geological perspective from the industry, Geological Society, London, Special Publications, 370, 17–37, https://doi.org/10.1144/SP370.14, 2012.

465 Carman, P. C.: Fluid flow through granular beds, Trans. Inst. Chem. Eng., 15, 150–166, 1937.

Carman, P. C.: Some physical aspects of water flow in porous media, Discussions of the Faraday Society, 3, 72, https://doi.org/10.1039/df9480300072, 1948.

Carman, P. C.: Flow of gases through porous media, Academic Press, 1956.

Chalikakis, K., Guérin, R., Valois, R., and Bosch, F.: Contribution of geophysical methods to karst-system exploration: an overview, Hydo-
470 geology Journal, 19, 1169–1180, https://doi.org/10.1007/s10040-011-0746-x, 2011.

Chen, Z., Goldscheider, N., Auler, A. S., and Bakalowicz, M.: The World karst aquifer mapping project: concept, mapping procedure and map of Europe, Hydrogeology Journal, 25, 771–785, https://doi.org/10.1007/s10040-016-1519-3, 2017.

Cherubini, A., Garcia, B., Cerepi, A., and Revil, A.: Influence of CO_2 on the electrical conductivity and streaming potential of carbonate rocks, Journal of Geophysical Research: Solid Earth, 124, 10 056–10 073, https://doi.org/10.1029/2018JB017057, 2019.

475 Choquette, P. W. and Pray, L. C.: Geologic nomenclature and classification of porosity in sedimentary carbonates, AAPG bulletin, 54, 207–250, https://doi.org/10.1306/5D25C98B-16C1-11D7-8645000102C1865D, 1970.

Clennell, B.: Tortuosity: a guide through the maze, Geological Society, London, Special Publications, 122, 299–344, https://doi.org/10.1144/GSL.SP.1997.122.01.18, 1997.

Costa, A.: Permeability-porosity relationship: A reexamination of the Kozeny-Carman equation based on a fractal pore-space geometry assumption, Geophysical Research Letters, 33, L02 318, https://doi.org/10.1029/2005GL025134, 2006.

Drew, D., Lamoreaux, P. E., Coxon, C., Wess, J. W., Slattery, L. D., Bosch, A. P., and Hötzl, H.: Karst hydrogeology and human activities: impacts, consequences and implications: IAH international contributions to hydrogeology 20, Drew, D. AND Hötzl, H., 5 edn., https://doi.org/10.1201/9780203749692, 2017.

Dullien, F. A. L.: 1 - Pore structure, in: Porous media (2nd edition), edited by Dullien, F. A. L., pp. 5–115, Academic Press, San Diego, https://doi.org/10.1016/B978-0-12-223651-8.50007-9, 1992.

Fabricius, I. L., Baechle, G., Eberli, G. P., and Weger, R.: Estimating permeability of carbonate rocks from porosity and vp vs, GEOPHYSICS, 72, E185–E191, https://doi.org/10.1190/1.2756081, 2007.

Ford, D. and Williams, P. D.: Karst hydrogeology and geomorphology, John Wiley & Sons, https://doi.org/10.1002/9781118684986, 2013.

Garcia-Rios, M., Luquot, L., Soler, J. M., and Cama, J.: The role of mineral heterogeneity on the hydrogeochemical response of two fractured reservoir rocks in contact with dissolved CO2, Applied Geochemistry, 84, 202–217, https://doi.org/10.1016/j.apgeochem.2017.06.008, 2017.

Garing, C., Luquot, L., Pezard, P., and Gouze, P.: Electrical and flow properties of highly heterogeneous carbonate rocks, AAPG Bulletin, 98, 49—-66, https://doi.org/10.1306/05221312134, 2014.

Ghanbarian, B.: Applications of critical path analysis to uniform grain packings with narrow conductance distributions: I. Single-phase permeability, Advances in Water Resources, 137, 103 529, https://doi.org/10.1016/j.advwatres.2020.103529, 2020.

Glover, P. W. J.: Geophysical properties of the near surface Earth: electrical properties, Treatise on Geophysics, https://doi.org/10.1016/B978-0-444-53802-4.00189-5, 2015.

Goldscheider, N., Meiman, J., Pronk, M., and Smart, C.: Tracer tests in karst hydrogeology and speleology, International Journal of speleology, 37, 27–40, https://doi.org/10.5038/1827-806X.37.1.3, 2008.

Golfier, F., Zarcone, C., Bazin, B., Lenormand, R., Lasseux, D., and Quintard, M.: On the ability of a Darcy-scale model to capture wormhole formation during the dissolution of a porous medium, Journal of Fluid Mechanics, 457, 213–254, https://doi.org/10.1017/S0022112002007735, 2002.

Guarracino, L., Rötting, T., and Carrera, J.: A fractal model to describe the evolution of multiphase flow properties during mineral dissolution, Advances in Water Resources, 67, 78–86, https://doi.org/10.1029/WR024i004p00566, 2014.

Gueguen, Y. and Dienes, J.: Transport properties of rocks from statistics and percolation, Mathematical Geology, 21, 1–13, https://doi.org/10.1007/BF00897237, 1989.

Hubbard, S. S. and Linde, N.: 2.15 - Hydrogeophysics, in: Treatise on Water Science, edited by Wilderer, P., pp. 401–434, Elsevier, Oxford, https://doi.org/10.1016/B978-0-444-53199-5.00043-9, 2011.

Izumoto, S., Huisman, J. A., Wu, Y., and Vereecken, H.: Effect of solute concentration on the spectral induced polarization response of calcite precipitation, Geophysical Journal International, 220, 1187–1196, https://doi.org/10.1093/gji/ggz515, 2020.

Izumoto, S., Huisman, J. A., Zimmermann, E., Heyman, J., Gomez, F., Tabuteau, H., Laniel, R., Vereecken, H., Méheust, Y., and Le Borgne, T.: Pore-scale mechanisms for spectral induced polarization of calcite precipitation inferred from geo-electrical millifluidics, Environmental Science & Technology, 56, 4998–5008, https://doi.org/10.1021/acs.est.1c07742, 2022.

Jackson, M. D.: Characterization of multiphase electrokinetic coupling using a bundle of capillary tubes model, Journal of Geophysical Research: Solid Earth, 113, https://doi.org/10.1029/2007JB005490, 2008.

Johnson, D., Koplik, J., and Schwartz, L.: New pore-size parameter characterizing transport in porous media, Physical Review Letters, 57, 2564–2567, 1986.

Jougnot, D., Jiménez-Martínez, J., Legendre, R., Le Borgne, T., Méheust, Y., and Linde, N.: Impact of small-scale saline tracer heterogeneity on electrical resistivity monitoring in fully and partially saturated porous media: Insights from geoelectrical milli-fluidic experiments, Advances in Water Resources, 113, 295–309, https://doi.org/10.1016/j.advwatres.2018.01.014, 2018.

Kaufmann, G. and Romanov, D.: Structure and evolution of collapse sinkholes: Combined interpretation from physico-chemical modelling and geophysical field work, Journal of Hydrology, 540, 688–698, https://doi.org/10.1016/j.jhydrol.2016.06.050, 2016.

Kačaroğlu, F.: Review of groundwater pollution and protection in karst areas, Water, Air, and Soil Pollution, 113, 337–356, https://doi.org/10.1023/A:1005014532330, 1999.

Kemna, A., Binley, A., Cassiani, G., Niederleithinger, E., Revil, A., Slater, L., Williams, K. H., Orozco, A. F., Haegel, F.-H., Hördt, A., Kruschwitz, S., Leroux, V., Titov, K., and Zimmermann, E.: An overview of the spectral induced polarization method for near-surface applications, Near Surface Geophysics, 10, 453–468, https://doi.org/10.3997/1873-0604.2012027, 2012.

Koohbor, B., Deparis, J., Leroy, P., Ataie-Ashtiani, B., Davarzani, H., and Colombano, S.: DNAPL flow and complex electrical resistivity evolution in saturated porous media: A coupled numerical simulation, Journal of Contaminant Hydrology, 248, 104 003, https://doi.org/10.1016/j.jconhyd.2022.104003, 2022.

Kozeny, J.: Uber kapillare leitung der wasser in boden, Royal Academy of Science, Vienna, Proc. Class I, 136, 271–306, 1927.

Leger, M. and Luquot, L.: Importance of microstructure in carbonate rocks: laboratory and 3D-imaging petrophysical characterization, Applied Sciences, 11, https://doi.org/10.3390/app11093784, 2021.

Leger, M., Luquot, L., and Roubinet, D.: Role of mineralogical, structural and hydrodynamic rock properties in conduits formation in three distinct carbonate rock types, Chemical Geology, p. 121008, https://doi.org/10.1016/j.chemgeo.2022.121008, 2022a.

Leger, M., Roubinet, D., Jamet, M., and Luquot, L.: Impact of hydro-chemical conditions on structural and hydro-mechanical properties of chalk samples during dissolution experiments, Chemical Geology, 594, 120 763, https://doi.org/10.1016/j.chemgeo.2022.120763, 2022b.

Leroy, P., Li, S., Revil, A., and Wu, Y.: Modelling the evolution of complex conductivity during calcite precipitation on glass beads, Geophysical Journal International, 209, 123–140, https://doi.org/10.1093/gji/ggx001, 2017.

Liñán Baena, C., Andreo, B., Mudry, J., and Carrasco Cantos, F.: Groundwater temperature and electrical conductivity as tools to characterize flow patterns in carbonate aquifers: The Sierra de las Nieves karst aquifer, southern Spain, Hydrogeology Journal, 17, 843–853, https://doi.org/10.1007/s10040-008-0395-x, 2009.

Lønøy, A.: Making sense of carbonate pore systems, AAPG bulletin, 90, 1381–1405, https://doi.org/10.1306/03130605104, 2006.

Lucia, F.: Petrophysical parameters estimated from visual descriptions of carbonate rocks: a field classification of carbonate pore space, Journal of Petroleum Technology, 35, 629–637, https://doi.org/10.2118/10073-PA, 1983.

Luquot, L. and Gouze, P.: Experimental determination of porosity and permeability changes induced by injection of CO_2 into carbonate rocks, Chemical Geology, 265, 148–159, https://doi.org/10.1016/j.chemgeo.2009.03.028, 2009.

Martys, N. S., Torquato, S., and Bentz, D. P.: Universal scaling of fluid permeability for sphere packings, Physical Review E, 50, 403–408, https://doi.org/10.1103/PhysRevE.50.403, publisher: American Physical Society, 1994.

Menke, H., Bijeljic, B., Andrew, M., and Blunt, M.: Dynamic three-dimensional pore-scale imaging of reaction in a carbonate at reservoir conditions, Environtal Science and Technology, 49, 4407–4414, https://doi.org/10.1021/es505789f, 2015.

Menke, H., Andrew, M., Blunt, M., and Bijeljic, B.: Reservoir condition imaging of reactive transport in heterogeneous carbonates using fast synchrotron tomography — effect of initial pore structure and flow conditions, Chemical Geology, 248, 15–26, https://doi.org/10.1016/j.chemgeo.2016.02.030, 2016.

555 Meyerhoff, S. B., Maxwell, R. M., Revil, A., Martin, J. B., Karaoulis, M., and Graham, W. D.: Characterization of groundwater and surface water mixing in a semi confined karst aquifer using time-lapse electrical resistivity tomography, Water Resources Research, 50, 2566–2585, https://doi.org/10.1002/2013WR013991, 2014.

Montanari, D., Minissale, A., Doveri, M., Gola, G., Trumpy, E., Santilano, A., and Manzella, A.: Geothermal resources within carbonate reservoirs in western Sicily (Italy): A review, Earth-Science Reviews, 169, 180–201, https://doi.org/10.1016/j.earscirev.2017.04.016, 2017.

560 Niu, Q. and Zhang, C.: Permeability prediction in rocks experiencing mineral precipitation and dissolution: a numerical study, Water Resources Research, 55, 3107–3121, https://doi.org/10.1029/2018WR024174, 2019.

Noiriel, C.: Resolving time-dependent evolution of pore-scale structure, permeability and reactivity using X-ray microtomography, Reviews in Mineralogy and Geochemistry, 80, 247–285, https://doi.org/10.2138/rmg.2015.80.08, 2015.

Noiriel, C., Gouze, P., and Bernard, D.: Investigation of porosity and permeability effects from microstructure changes during limestone
565 dissolution, Geophysical Research Letters, 31, L24 603, https://doi.org/10.1029/2004GL021572, 2004.

Noiriel, C., Bernard, D., Gouze, P., and Thibault, X.: Hydraulic properties and micro-geometry evolution accompanying limestone dissolution by acidic water, Oil and Gas Science and Technology, 60, 177–192, https://doi.org/10.2516/ogst:2005011, 2005.

Pape, H., Clauser, C., and Iffland, J.: Permeability prediction based on fractal pore-space geometry, GEOPHYSICS, 64, 1447–1460, https://doi.org/10.1190/1.1444649, 1999.

570 Paterson, M.: The equivalent channel model for permeability and resistivity in fluid-saturated rock—A re-appraisal, Mechanics of Materials, 2, 345–352, https://doi.org/10.1016/0167-6636(83)90025-X, 1983.

Pereira Nunes, J., Blunt, M., and Bijeljic, B.: Pore-scale simulation of carbonate dissolution in micro-CT images, Journal of Geophysical Research: Solid Earth, 121, 558–576, 2016.

Rembert, F., Jougnot, D., and Guarracino, L.: A fractal model for the electrical conductivity of water-saturated porous media during mineral
575 precipitation-dissolution processes, Advances in Water Resources, 145, 103 742, https://doi.org/10.1016/j.advwatres.2020.103742, 2020.

Rembert, F., Jougnot, D., Luquot, L., and Guérin, R.: Interpreting Self-Potential Signal during Reactive Transport: Application to Calcite Dissolution and Precipitation, Water, 14, 1632, https://doi.org/10.3390/w14101632, 2022.

Revil, A., Karaoulis, M., Johnson, T., and Kemna, A.: Some low-frequency electrical methods for subsurface characterization and monitoring in hydrogeology, Hydrogeology Journal, 20, 617–658, https://doi.org/10.1007/s10040-011-0819-x, 2012.

580 Revil, A., Kessouri, P., and Torres-Verdin, C.: Electrical conductivity, induced polarization, and permeability of the Fontainebleau sandstone, Geophysics, 79, D301–D318, https://doi.org/10.1190/geo2014-0036.1, 2014.

Rötting, T., Luquot, L., Carrera, J., and Casalinuovo, D. J.: Changes in porosity, permeability, water retention curve and reactive surface area during carbonate rock dissolution, Chemical Geology, 403, 86–98, https://doi.org/10.1016/j.chemgeo.2015.03.008, 2015.

Saneiyan, S., Ntarlagiannis, D., Ohan, J., Lee, J., Colwell, F., and Burns, S.: Induced polarization as a monitoring tool for in-situ microbial
585 induced carbonate precipitation (MICP) processes, Ecological Engineering, 127, 36–47, https://doi.org/10.1016/j.ecoleng.2018.11.010, 2019.

Saneiyan, S., Ntarlagiannis, D., and Colwell, F.: Complex conductivity signatures of microbial induced calcite precipitation, field and laboratory scales, Geophysical Journal International, 224, 1811–1824, https://doi.org/10.1093/gji/ggaa510, 2021.

Soldi, M., Guarracino, L., and Jougnot, D.: A simple hysteretic constitutive model for unsaturated flow, Transport in Porous Media, 120, 271–285, https://doi.org/10.1007/s11242-017-0920-2, 2017.

Soldi, M., Guarracino, L., and Jougnot, D.: The effect of pore geometry in constitutive hysteretic models for unsaturated water flow, Environmental Fluid Mechanics, 22, 1283–1305, https://doi.org/10.1007/s10652-022-09891-0, 2022.

Sun, Z., Mehmani, A., and Torres-Verdín, C.: Pore-scale investigation of the electrical resistivity of saturated porous media: flow patterns and porosity efficiency, Journal of Geophysical Research: Solid Earth, 126, e2021JB022 608, https://doi.org/10.1029/2021JB022608, 2021.

Thanh, L., Jougnot, D., Phan, V., and Nguyen, V.: A physically based model for the electrical conductivity of water-saturated porous media, Geophysical Journal International, 219, 866–876, https://doi.org/10.1093/gji/ggz328, 2019.

Thompson, A., Katz, A., and Krohn, C.: The microgeometry and transport properties of sedimentary rock, Advances in Physics, 36, 625–694, https://doi.org/10.1080/00018738700101062, 1987.

Torquato, S. and Lu, B.: Chord-Length Distribution Function for Two-Phase Random Media, Physical Review E, 47, 2950, https://doi.org/10.1103/PhysRevE.47.2950, 1993.

Vialle, S., Contraires, S., Zinzsner, B., Clavaud, J. B., Mahiouz, K., Zuddas, P., and Zamora, M.: Percolation of CO2-rich fluids in a limestone sample: Evolution of hydraulic, electrical, chemical, and structural properties, Journal of Geophysical Research: Solid Earth, 119, 2828–2847, https://doi.org/10.1002/2013JB010656, 2014.

Vinogradov, J., Hill, R., and Jougnot, D.: Influence of pore size distribution on the electrokinetic coupling coefficient in two-phase flow conditions, Water, 13, 2316, https://doi.org/10.3390/w13172316, 2021.

Walsh, J. B. and Brace, W. F.: The effect of pressure on porosity and the transport properties of rock, Journal of Geophysical Research, 89, 9425, https://doi.org/10.1029/JB089iB11p09425, 1984.

Weger, R. J., Eberli, G. P., Baechle, G. T., Massaferro, J. L., and Sun, Y.-F.: Quantification of pore structure and its effect on sonic velocity and permeability in carbonates, AAPG Bulletin, 93, 1297–1317, https://doi.org/10.1306/05270909001, 2009.

Winsauer, W. O., Shearin, H. M., J., Masson, P. H., and Williams, M.: Resistivity of brine-saturated sands in relation to pore geometry, AAPG Bulletin, 36, 253–277, https://doi.org/10.1306/3D9343F4-16B1-11D7-8645000102C1865D, 1952.

Wu, Y., Hubbard, S., Williams, K. H., and Ajo-Franklin, J.: On the complex conductivity signatures of calcite precipitation, Journal of Geophysical Research, 115, G00G04, https://doi.org/10.1029/2009JG001129, 2010.

Yu, B., Li, J., Li, Z., and Zou, M.: Permeabilities of unsaturated fractal porous media, International Journal of Multi-phase Flow, 29, 1625–1642, https://doi.org/10.1016/S0301-9322(03)00140-X, 2003.

Zhang, C., Slater, L., Redden, G., Fujita, Y., Johnson, T., and Fox, D.: Spectral induced polarization signatures of hydroxide adsorption and mineral precipitation in porous media, Environmental Science & Technology, 46, 4357–4364, https://doi.org/10.1021/es204404e, 2012.